Communications in Computational Chemistry
Commun. Comput. Chem., Vol. 7, No. 3, 171–180
doi: 10.4208/cicc.2025.97.01
Regular Article

Evaluating Nirmatrelvir Resistance in SARS-CoV-2 Main Protease: A Comparison Between MM/PBSA and Free Energy Perturbation

Xiaoxiao Lyu[1] and Ye Mei[1, 2, 3]

[1]*State Key Laboratory of Precision Spectroscopy, School of Physics and Electronic Science, East China Normal University, Shanghai 200241, China*;

[2]*NYUE-CNU Center for Computational Chemistry at NYU Shanghai, Shanghai 200062, China*;

[3]*Collaborative Innovation Center of Eatreme Optics, Shanxi University, Taiyuan, Shanxi 030006, China.*

* Corresponding authors: ymei@phy.ecnu.edu.cn (Ye Mei)

Received on 6 May 2025; Accepted on 2 June 2025

Abstract: Mutations that cause structural changes in proteins can sometimes reduce drug efficacy dramatically, a phenomenon known as mutation-induced drug resistance. For example, emerging drug-resistant mutations in the SARS-CoV-2 main protease (M^{pro}) threaten the long-term efficacy of nirmatrelvir, the active component of Paxlovid. Various methods have been developed to predict the impact of such mutations, with differing levels of reliability. In this study, comparative binding free energy calculations using Molecular Mechanics/Poisson–Boltzmann Surface Area (MM/PBSA) and Alchemical Transformation (also known as Free Energy Perturbation, or FEP) were performed to assess five naturally occurring M^{pro} mutations (SER144ALA, MET165ALA, GLU166ALA, HIE172ALA, and GLN192ALA) at the nirmatrelvir binding site. The results reveal a weak correlation ($R_{Pearson}$ = 0.18) between MM/PBSA predictions and experimental data. In contrast, FEP calculations using either the Multistate Bennett Acceptance Ratio (MBAR) or Thermodynamic Integration (TI) yield stronger linear correlations ($R_{Pearson}$ = 0.56 and 0.57, respectively). This study highlights the superior reliability of FEP in quantifying binding affinity losses due to drug resistance and underscores its potential for the proactive surveillance of clinical resistance mutations. Moreover, such insights are crucial for advancing antiviral drug development and guiding the design of inhibitors with a reduced risk of resistance evolution.

Key words: drug resistance, MM/PBSA, free energy perturbation, alchemical transformation, binding affinity.

1. Introduction

The emergence of antiviral resistance is prevalent in the treatment of chronic or persistent viral infections, including human immunodeficiency virus (HIV), hepatitis B virus (HBV), hepatitis C (HCV), herpesviruses, and influenza [1]. In these cases, prolonged antiviral therapy, particularly as monotherapy, has driven the selection of viral escape mutations, consequently reducing therapeutic efficacy and leading to treatment failure [2-4]. Resistance to protease inhibitors arises from amino acid substitutions occurring either within the substrate-binding pocket

or at distal sites. At the molecular level, this resistance is primarily driven by a significant reduction in the binding affinity of the inhibitor for mutated protease, while substrate binding remains largely unaffected [5]. This change in affinity can be quantitatively assessed through binding free energy calculations. Various methods have been proposed for the calculations of binding free energies between ligands and their target proteins. Among these, Molecular Mechanics/Poisson-Boltzmann Surface Area (MM/PBSA) and Alchemical Transformations (also known as Free Energy Perturbation or FEP hereafter) methods are the most widely used in both academia and industry today [6-9]. However, each method has its own advantages and disadvantages in terms of the accuracy and computational cost.

Since December 2019, the COVID-19 pandemic caused by SARS-CoV-2 has severely impacted global health [10-12]. SARS-CoV-2 Main Protease (M^{pro}) plays a crucial role in viral replication by cleaving the viral polyproteins pp1a and pp1ab at 11 distinct sites, thereby generating nonstructural proteins essential for the viral lifecycle [4,13,14]. From an evolutionary perspective, the amino acid sequence and three-dimensional structure of M^{pro} are highly conserved across the subfamily *Coronavirinae*, providing a strong mechanistic foundation for the development of therapeutics, particularly in response to emerging SARS-CoV-2 variants with potential immune evasion concerns [10,15,16]. Moreover, the absence of a homologous protease in humans enhances the specificity and safety of targeting Mpro, making it an attractive and promising drug target for antiviral therapy development [17-21].

Pfizer's oral drug Paxlovid which combines the M^{pro} inhibitor nirmatrelvir and its metabolic enhancer ritonavir was granted Emergency Use Authorization by the FDA in December of 2021. Nirmatrelvir (PF-07321332) has been shown to be a highly effective inhibitor of M^{pro}, with an IC_{50} of 4 nM. Meanwhile, nirmatrelvir exhibits an extraordinary level of selectivity against a panel of human proteases, with submicromolar activity observed only for cathepsin K (IC_{50} = 231 nM), underscoring its potential as a therapeutic agent with minimal off-target effects [10,22]. The active site of SARS-CoV-2 M^{pro} features a non-canonical catalytic dyad, Cys145-His41, where the Sγ atom of Cys145 forms a reversible C-S covalent bond with the nitrile carbon of nirmatrelvir. In a study by Zhao *et al* [10]., the electron density map captured dual conformations of the catalytic cysteine, further supporting the reversibility of the covalent bond. Early administration of nirmatrelvir in COVID-19 reduces viral load and decreases the risk of progression to severe disease [23,24]. The ease of oral administration of nirmatrelvir further establishes it as a favorable option for high-risk patients [4].

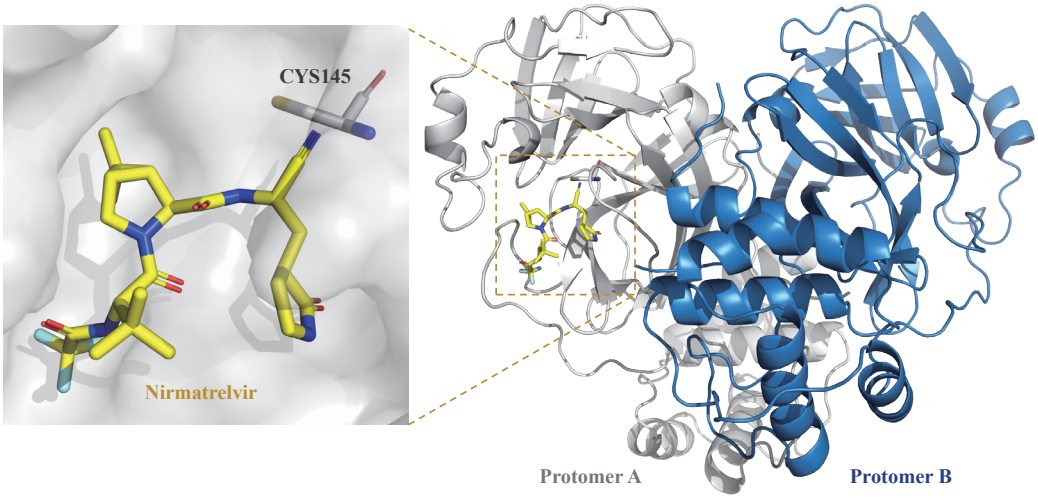

Figure 1: Nirmatrelvir (depicted as sticks) in complex with SARS-CoV-2 M^{pro}. The M^{pro} dimer is illustrated using a cartoon representation, with the two subunits colored gray and blue.

However, the emergence of drug resistance mutations in Mpro raises the concern of possible alter susceptibility of nirmatrelvir and threaten the long-term effectiveness as an antiviral treatment for potential future pandemic. Several studies have reported the emergence of nirmatrelvir-resistant M^{pro} mutants through viral passage experiments. Mutations in residues SER144, GLU166, and ALA173 have direct impact on nirmatrelvir inhibition [25-29].

In this study, MM/PBSA and FEP were applied to calculate the binding free energies of nirmatrelvir with Mpro mutants (SER144ALA, MET165ALA, GLU166ALA, HIE172ALA, and GLN192ALA), as well as the wild-type M^{pro}. These mutants were selected based on prior experimental evidence indicating their role in conferring resistance to nirmatrelvir [29]. Accordingly, the correlation between the calculated binding free energies and experimental affinity values was evaluated using the Pearson correlation coefficient. Notably, only the binding energy differences along the sequence were examined, and entropy contributions were assumed to be invariant across the protein variants and thus were omitted in the MM/PBSA calculations. The Pearson correlation coefficient of 0.18 from the MM/PBSA calculations shows a weak linear correlation with the experimental data. In contrast, FEP calculations using MBAR and TI for the alchemical transformation analysis yield correlation coefficients of 0.56 and 0.57, respectively, indicating a better agreement with the experimental data. The study suggests that the FEP calculations strongly correlate with experimental results, highlighting the potential of the FEP method as a powerful tool for providing accurate affinity values between protein and ligand, particularly when considering binding energy differences along the sequence. Meanwhile, the MM/PBSA calculations remain valuable (probably for pre-screening) due to their lower computational cost, especially when precise agreement with experimental absolute affinities is not critical.

2. Method

2.1 Prepartion of the molecular mystems

The initial coordinates of the protein-ligand complex were obtained from the 1.59 Å resolution crystal structure (PDB ID: 7VH8) in the Protein Data Bank [10]. The M^{pro} monomer is intrinsically inactive, whereas its biologically active form is a homodimer, with the two subunits arranged nearly orthogonally. The dimer structure was constructed using PyMOL (Schr¨odinger, LLC) by utilizing the C_2 symmetry [30]. The crystal structure reveals two conformational states of Cys145. In the dominant state (80% occupancy), the sulfur atom of Cys145 forms a covalent bond with the nitrogen atom of the imine group in the ligand molecule. In the alternative state, with 20% occupancy, the sulfur atom of Cys145 engages in a hydrogen bond with the nitrogen atom of the nitrile warhead of ligand nirmatrelvir. Since the populations of the covalent and noncovalent binding states differ by only 4 folds, the binding free energies have only a small difference in magnitude. As shown in Fig. 1, this study selected the noncovalent state of Cys145 to investigate the binding interaction between M^{pro} and nirmatrelvir prior to proton transfer from Cys145 to His41. To facilitate this transfer, the imidazole ring of His41 was rotated to orient the ϵ-nitrogen toward the sulfur atom of Cys145, creating a geometrically favorable protonation pathway. The nitrile warhead of nirmatrelvir was modified and all hydrogen atoms were subsequently added using the Discovery Studio Visualizer [31]. The free ligand nirmatrelvir was optimized using Gaussian 16 [32] at the B3LYP/6-31G(d) level. The Generalized AMBER Force Field version 2 (GAFF2)[33] and AM1-BCC partial charges [34,35] were assigned to the nirmatrelvir molecule. The M^{pro} topology parameters were generated using the AMBER14SB force field [36]. All crystal water molecules were kept. The Mpro-nirmatrelvir complex was solvated in a TIP3P37 water box with a minimum distance of 15 Å between the complex and the boundary of the unit cell, using the LEaP module in AmberTools24 [38]. Finally, the system was neutralized and ionized with sodium and chloride ions to maintain a physiological salt concentration of 150 mM.

2.2 Simulation protocols

Prior to conducting MM/PBSA and FEP calculations for all complexes, the systems are equilibrated to ensure structural relaxation. The simulation protocol for each complex system consists of the following steps. First, energy minimization is performed for a total of 10,000 steps, comprising 5,000 steps of the steepest descent algorithm followed by 5,000 steps of the conjugate gradient optimization algorithm. During this stage, positional restraints are applied to heavy atoms using a restraining force constant of 5 kcal/mol/Å^2. This is followed by an additional 10,000 steps of minimization, again consisting of 5,000 steps of steepest descent and 5,000 steps of conjugate gradient optimization, but without positional restraints. Subsequently, the system is gradually heated from 5 K to 298.15 K, regulated by a Langevin thermostat with a collision frequency of 2.0 ps^{-1}. Then, the heated system is simulated in NPT simulation for 500 ps, with positional restraints applied to heavy atoms, using a restraining force constant 10 kcal/mol/Å^2. Finally, the equilibrated system was simulated under NPT conditions for 100 ns on GPUS without positional restraints. The SHAKE algorithm [39] was applied to constrain covalent bonds involving hydrogen atoms, allowing a time step of 2 fs in all simulations. Electrostatic and van der Waals (vdW) interactions were truncated at 12.0 Å in real space, while the long-range electrostatic interaction were computed using the particle mesh Ewald (PME) method [40,41] Snapshots were extracted every 100 ps from the 100 ns equilibrated simulation for MM/PBSA calculations. The relaxed structure from each simulation is used as the starting point for subsequent FEP calculations.

2.3 Theoretical background of MM/PBSA

As illustrated in Fig. 2A, MM/PBSA methods [42-45] have become widely adopted for estimating binding free energies. MM/PBSA method utilize implicit solvation models to calculate solvation energy, providing a computationally efficient alternative due to their low computational cost and ease of implementation [46] Extensive and detail explanation of the terms involved in MM/PBSA calculations can be found elsewhere [47-50], and only a brief introduction is provided here. In the general, the binding free energy of the protein with ligand in solvent can be expressed as

$$\Delta G_{\text{binding}} = G_{\text{complex}} - G_{\text{protein}} - G_{\text{ligand}}, \quad (1)$$

where G_{complex}, G_{protein} and G_{ligand} are the total free energies of the protein-ligand complex, the isolated protein, and the ligand in solvent, respectively. The free energy of each individual entity, G, can be expressed as:

$$G = E_{\text{gas}} + G_{\text{solvation}} - TS_{\text{solute}}, \quad (2)$$

in which E_{gas} is the gas-phase energy, $G_{\text{solvation}}$ is the solvation free energy, and TS is the entropic contribution [51]. The gas phase energy is usually calculated at the molecular mechanics level as

$$E_{\text{gas}} = E_{\text{MM}} = E_{\text{bond}} + E_{\text{angle}} + E_{\text{dihedral}} + E_{\text{vdw}} + E_{\text{coulomb}}, \quad (3)$$

and the solvation free energy (ΔG_{solv}) is conventionally decomposed into polar (ΔG_{polar}) and nonpolar ($\Delta G_{\text{nonpolar}}$) contributions:

$$\Delta G_{\text{solv}} = \Delta G_{\text{polar}} + \Delta G_{\text{nonpolar}}, \quad (4)$$

where ΔG_{polar} is estimated by solving the Poisson-Boltzmann (PB) equation [52-54]. Nonpolar contributions are often estimated using the solvent-accessible surface area (SASA), one of the most widely used nonpolar models.55 The SASA model assumes a linear dependence of the nonpolar free energy term (Gnonpolar) on the solvent-accessible surface area

$$G_{\text{nonpolar}} = \gamma A + b, \quad (5)$$

where γ is the coefficient associated with the solvent surface tension, A represents the SASA, and b is the offset [49]. Taking together, the binding free energy can be written in an ensemble form as

$$\Delta G_{\text{binding}} = \langle \Delta E_{\text{gas}} \rangle + \langle \Delta G_{\text{solvation}} \rangle - T\langle \Delta S_{\text{solute}} \rangle. \quad (6)$$

In this study, the MM/PBSA protocol was adopted while neglecting the solute entropic contribution, as our primary focus is the differences in the binding free energies caused by mutations. The

entropic contribution is typically estimated using quasi-harmonic or normalmode analysis [56]. However, it is often omitted due to the high computational cost required for fully sampling the free energy landscape, and its inclusion remains controversial [57-59].

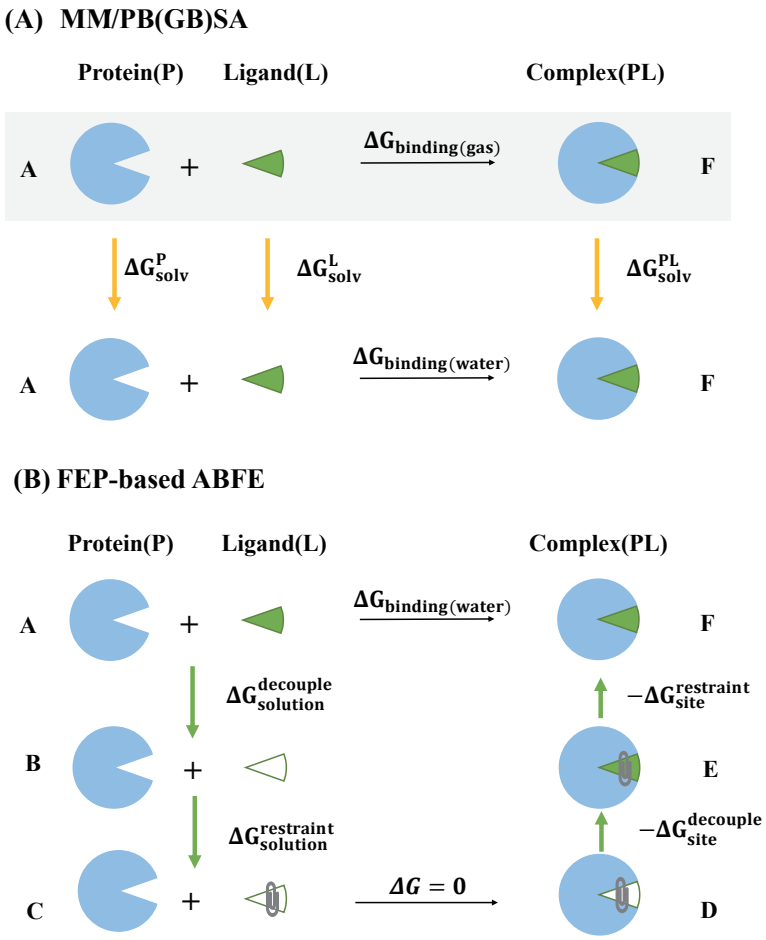

Figure 2. (A). Thermodynamic cycle used for MM/PBSA calculations. The protein, ligand, and their complex within the gray rectangle indicate a vacuum environment. (B). Thermodynamic cycle used in FEP-based absolute binding free energy (ABFE) calculations, with the paperclip symbol indicating the application of restraints. The green ligand signifies the presence of Coulombic and van der Waals interactions with the environment, while the white ligand represents a state in which its interactions with the environment are turned off.

2.4 Theoretical background of FEP

The workflow for calculating absolute binding free energy follows the well-established thermodynamic cycle, employing the widely adopted double decoupling method (DDM), as illustrated in Fig. 2B [60-67]. As the name suggests, DDM involves sequentially turning off (decoupling) van der Waals (vdW) and electrostatic interactions between the ligand and its environment in both the bulk solvent and the binding pocket. The corresponding free energy changes are denoted as $\Delta G_{\text{solution}}^{\text{decouple}}$ and $\Delta G_{\text{site}}^{\text{decouple}}$, respectively. During the decoupling of the ligand from its environment in the binding site, additional harmonic restraints, also known as the Boresch-style restraints, are applied on the translational and rotational degrees of freedom of the ligand molecule, thereby preventing it from wandering around, which may otherwise slow down the convergence. $\Delta G_{\text{site}}^{\text{restraint}}$ is the free energy of removing the Boreschstyle restraints between the fully interacting ligand and the protein in the binding site. Its counterpart in aqueous solution $\Delta G_{\text{solution}}^{\text{restraint}}$ can be computed analytically [63,65]. Following the alchemical transformation path above, the calculated binding free energy can be written as

$$\Delta G_{\text{binding}} = \Delta G_{\text{solution}}^{\text{decouple}} + \Delta G_{\text{solution}}^{\text{restraint}} - \Delta G_{\text{site}}^{\text{decouple}} + \Delta G_{\text{site}}^{\text{restraint}}. \quad (7)$$

For the alchemical double decoupling process, van der Waals (vdW) and electrostatic interactions are turned off simultaneously using their respective softcore potentials [68,69]. In the bulk solvent, the nonbond interaction potentials are turned off with λ taking the sequential values (0.0, 0.01, 0.025, 0.05, 0.075, 0.1, 0.15, 0.2, 0.3, 0.4, 0.5, 0.6, 0.65, 0.7, 0.75, 0.8, 0.85, 0.9, 0.95, 1.0). To ensure reasonable phase overlap and comparable computational cost, the λ schedule in the binding pocket generally follows the same sequence as in bulk solvent: (0.0, 0.01, 0.025, 0.05, 0.075, 0.1, 0.15, 0.2, 0.3, 0.4, 0.5, 0.6, 0.65, 0.7, 0.75, 0.8, 0.85, 0.9, 0.95, 1.0). For the wild-type M^{pro}-nirmatrelvir complex, an additional window at λ = 0.525 was introduced to improve phase-space overlap, resulting in a 21-λ schedule: (0.0, 0.01, 0.025, 0.05, 0.075, 0.1, 0.15, 0.2, 0.3, 0.4, 0.5, 0.525, 0.6, 0.65, 0.7, 0.75, 0.8, 0.85, 0.9, 0.95, 1.0). For the HIE172ALA M^{pro}-nirmatrelvir complex, two additional windows at λ = 0.550 and λ = 0.625 were added, giving a 22-λ schedule: (0.0, 0.01, 0.025, 0.05, 0.075, 0.1, 0.15, 0.2, 0.3, 0.4, 0.5, 0.55, 0.6, 0.625, 0.65, 0.7, 0.75, 0.8, 0.85, 0.9, 0.95, 1.0). For the nirmatrelvir complexes with the SER144ALA, MET165ALA, GLU166ALA,

and GLN192ALA M^{pro} mutants, the 20-λ schedule was used without modification. During ligand decoupling in the binding site, three heavy atoms of the ligand and the α-carbon atoms of three protein residues are selected for defining the Boresch-style restraints, with force constants of 10 kcal/mol/Å^2, 100 kcal/mol/rad^2, and 100 kcal/mol/rad^2 for bond, angle, and dihedral terms, respectively. These restraints are gradually removed with λ values (0.0, 0.01, 0.025, 0.05, 0.075, 0.1, 0.15, 0.2, 0.35, 0.5, 0.75, 1.0). All the simulations are carried out with AMBER24. Parameters related to GPU-accelerated thermodynamic integration (GTI)[70,71] and softcore potentials are applied with default settings.

For each window with the λ value held constant throughout the simulation, energy minimization is performed in two stages. The first stage consists of 10,000 steps (5,000 steps of steepest descent followed by 5,000 steps of conjugate gradient optimization) with positional restraints applied to heavy atoms using a force constant of 5 kcal/mol/Å^2. In the second stage, 10,000 additional steps (5,000 steepest descent and 5,000 conjugate gradient) are performed without positional restraints. After minimization, the system is heated from 5 K to 298.15 K, regulated by a Langevin thermostat with a collision frequency of 2.0 ps^{-1}. Then, a 500 ps NPT equilibration is performed with positional restraints applied to heavy atoms using a force constant of 5 kcal/mol/Å^2, followed by 100 ps of unrestrained NPT equilibration. Next, a 5 ns production simulation is performed under NPT conditions without restraints, utilizing GPUs via pmemd.cuda. Electrostatic and van der Waals (vdW) interactions are truncated at 12Å in real space, and long-range electrostatics are computed using the particle mesh Ewald (PME) method [40, 41]. The integration timestep is set to 1 fs, and snapshots are saved every 1 ps during the production phase. The final 4 ns of production trajectories are post-processed to calculate free energy differences using the Multistate Bennett Acceptance Ratio (MBAR) method [72-74], which is known for its low asymptotic variance. To estimate uncertainties, three independent simulations are conducted for nirmatrelvir bound to the wild-type M^{pro} and its variants (SER144ALA, MET165ALA, GLU166ALA, HIE172ALA, and GLN192ALA). Thermodynamic Integration (TI) is also applied and is used for consistency check with MBAR.

3. Results and discussion

The interaction between the wild-type M^{pro} and nirmatrelvir was analyzed to investigate the role of the residues to be mutated. Several hydrogen bonds are formed between nirmatrelvir and the protein. As shown in Table S1, GLU166 plays a pivotal role in the binding pocket, serving as both a donor and an acceptor in hydrogen bonding. Specifically, the O3 atom of nirmatrelvir forms a hydrogen bond with the main chain nitrogen atom of GLU166, while the main chain oxygen atom of GLU166 forms a hydrogen bond with the N5 atom of nirmatrelvir. These interactions are highly stable, with a survival rate exceeding 98% over a 100-ns simulation. Additionally, the N4 atom of nirmatrelvir donates a hydrogen bond to the main chain oxygen atom of HIE164, while the NE2 atom of HIE163 donates a hydrogen bond to the O1 atom of nirmatrelvir. The nitrogen atom of CYS145 donates a hydrogen bond to the N1 atom of nirmatrelvir, and the nitrogen atom of THR190 donates a hydrogen bond to the O4 atom of nirmatrelvir. All these hydrogen bonds have a survival rate greater than 40%.

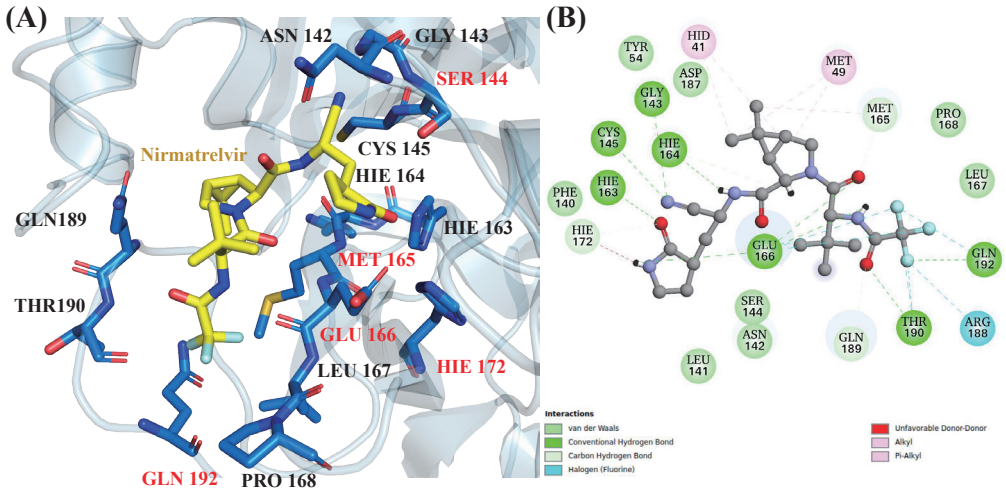

Figure 3. (A). A close-up view of the wild-type M^{pro} interacting with Nirmatrelvir. The residue labels in red correspond to the mutations studied (SER144ALA, MET165ALA, GLU166ALA, HIE172ALA, and GLN192A). (B). A 2D representation of the interaction between Nirmatrelvir and M^{pro}.

Mutations in key residues such as SER144ALA,MET165ALA, GLU166ALA, HIE172ALA, and GLN192ALA (as shown in Fig. 3) within the binding pocket directly influence nirmatrelvir inhibition. The binding free energies between the mutated M^{pro} and nirmatrelvir were calculated using the MM/PBSA and FEP based ABFE methods. This analysis was complemented by calculating the binding free energy of the wild-type M^{pro}-nirmatrelvir complex to assess how these mutations disrupt binding affinity.

The binding free energy of nirmatrelvir in complex with wild-type M^{pro} was calculated using the MM/PBSA method on snapshots taken every 100 ps from a 100-ns equilibrated simulation. As shown in Fig. 4A, the wild-type complex displays stable behavior, with RMSD values remaining consistently below 3 Å, indicating a well-behaved structure that has likely reached proper equilibration. Similarly, for each mutant variant (SER144ALA, MET165ALA, GLU166ALA, HIE172ALA, and GLN192ALA), the M^{pro} -nirmatrelvir complex also reaches equilibrium, as evidenced by RMSD values in their respective figures (Fig. 4B-F). These findings suggest that while mutations may alter local binding interactions, the overall complexes remain stable over the simulation period.

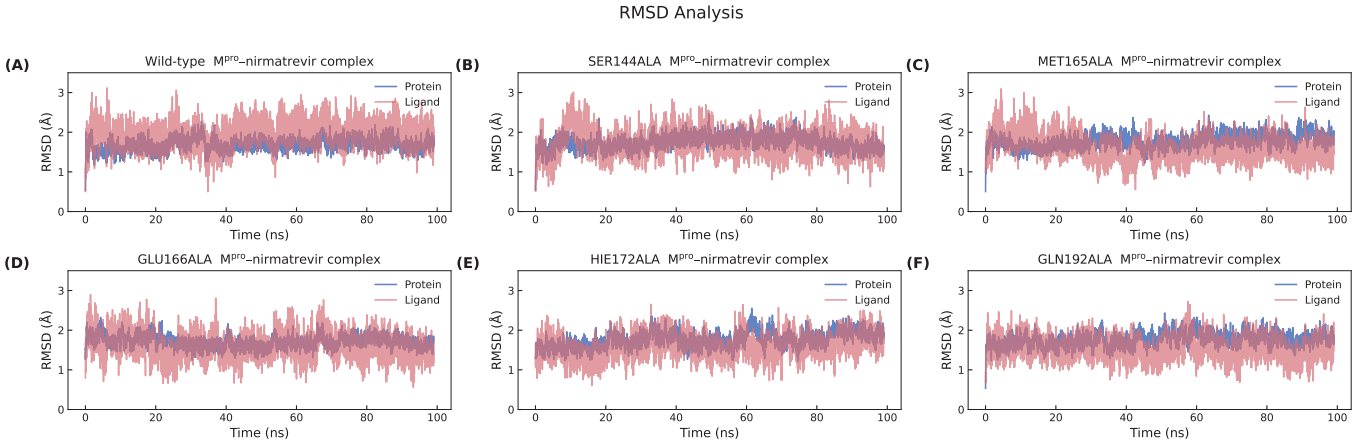

Figure 4. Root-mean-square deviation (RMSD) analysis of the 100-ns equilibrium simulations for the complexes of nirmatrelvir with the wild-type M^{pro} and its mutants (SER144ALA, MET165ALA, GLU166ALA, HIE172ALA, and GLN192ALA).

To assess the reliability of the FEP method, convergence analysis of free energy simulations was visualized and plotted using the alchemlyb software, following the guidelines established by Klimovich *et al* [75]. As illustrated in Fig. S1, example plots are provided for the alchemical transformation substage simulations of the decoupling free energy $\Delta G_{site}^{decouple}$, corresponding to the complex calculation of the molecule nirmatrelvir bound to the wild-type M^{pro}. The computed free energy differences (with error bars) are visualized as a function of simulation time in Fig. S1A to assess equilibration and convergence. The forward and reverse free energy estimates, derived from equilibrium trajectory snapshots, exhibit partial reflection symmetry around the final value ΔG_{final} and converge from opposite directions. Once the system reaches full equilibration, these forward and reverse free energy estimates agree within statistical uncertainty. As shown in Fig. S1A, the calculations have approximately converged around t = 0.8 of the total simulation time. To assess phase space overlap, the distribution of energy differences between neighboring windows is plotted (Fig. S1D). The overlap matrix, also visualized in this figure, is crucial for accurate free energy calculations. It should be at least tridiagonal with nonzero elements along the main and adjacent diagonals to ensure reliable results. Values below 0.03 indicate insufficient overlap. As shown in Fig. S1D, the criterion is satisfied, ensuring reliable results. Meanwhile, as shown in Fig. S1B, the plot of $\langle \frac{\partial U}{\partial \lambda} \rangle$ versus λ for thermodynamic integration displays a smooth variation in slope, validating the chosen λ settings. The filled areas represent free energy estimates obtained using the trapezoidal rule, with color intensity varying by λ index. Moreover, Comparing MBAR and TI results can help identify insufficient sampling or overly wide λ spacing. As shown in Fig. S1C both methods yield similar free energy differences between adjacent states, with error estimates provided. Similarly, Fig. S2 to Fig. S6 show the alchemical transformation substage simulations of the decoupling free energy $\Delta G_{site}^{decouple}$ for the nirmatrelvir-SER144ALA, MET165ALA, GLU166ALA, HIE172ALA, and GLN192ALA M^{pro} complexes, respectively. In summary, all FEP results in this study underwent these consistency checks, helping to identify convergence issues, sampling problems, and other potential pitfalls, thereby bolstering the reliability of the FEP results.

Figure 5A highlights significant differences between MM/PBSA and experimental values. MM/PBSA estimates significantly overestimate the binding free energy compared to experimental values, which range from -12 to -9 kcal/mol, while computed values fall between -50 and -40 kcal/mol. This notable discrepancy is attributed primarily to the omission of entropic contributions in the MM/PBSA calculations. Conversely, as shown in Fig. 5B and

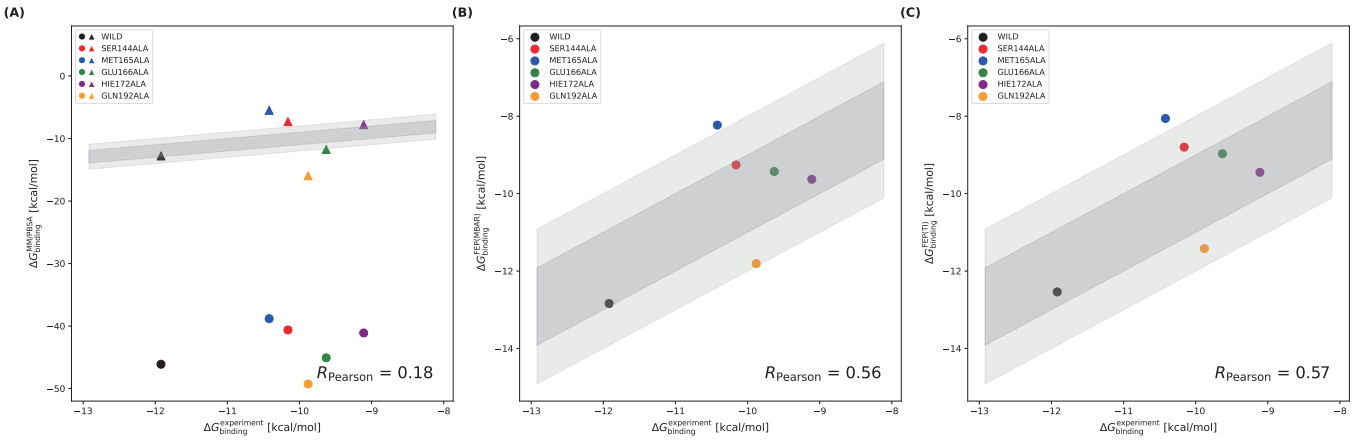

Figure 5. (A) Comparison of predicted (A) MM/PBSA binding free energies, (B) FEP (MBAR) binding free energies and (C) FEP (TI) binding free energies with experimental values for complex systems. The deviation bounds of 1 kcal/mol and 2 kcal/mol are represented by the gray and light-gray regions, respectively. In (A), the original data (round dots) are systematically shifted (triangle) during fitting.

C, FEP calculations processed with MBAR and TI exhibit strong agreement with experimental data. For the mutations SER144ALA, GLU166ALA, HIE172ALA, and GLN192ALA, the computed results deviate by no more than 2 kcal/mol from the measured values. Notably, HIE172ALA and GLU166ALA show deviations within 1 kcal/mol from the experimental data, while MET165ALA diverges slightly above 2 kcal/mol. All detailed values comparing the MM/PBSA and FEP calculations with experimental data, including uncertainty estimates, are presented in Table S2 of the supporting information.

As shown in Table 1, the analysis of the hydrogen bonds between M^{pro} and nirmatrelvir with a survival rate greater than 0.5 in the molecular dynamics simulations provides insights into the mechanistic basis of changes in binding affinity. In the wild-type M^{pro}-nirmatrelvir complex, fiveM^{pro} atoms-GLU166@N, GLU166@O, HIE164@O, HIE163@NE2, and CYS145-@N-form stable hydrogen bonds with nirmatrelvir. The MD simulations of the mutated M^{pro}-nirmatrelvir complexes reveals differential binding patterns. In the SER144ALA mutant, hydrogen bonds involving GLU166@N, GLU166@O, and HIE163@NE2 are retained, whereas those with HIE164@O and CYS145@N disappear, reducing the total number of stable hydrogen bonds to three. For the MET165ALA and GLN192ALA mutants, the interactions involving GLU166@N, GLU166@O, and HIE163@NE2 are retained, while the hydrogen bonds with HIE164@O and CYS145@N are substituted by THR190@N. For the GLU166ALA mutant, the hydrogen bond donors/acceptors GLU166@N and GLU166@O are replaced by ALA166@N and ALA166@O. Additionally, the bonds with HIE164@O and CYS145@N are substituted by PHE140@O. In the HIE172ALA mutant, the hydrogen bondinvolving CYS145@N disappears. In summary, the mutations alter the native binding pattern, reduce the number of stable hydrogen bonds, and thereby contribute to the observed losses in binding affinity.

Table 1. Hydrogen bonds with a survival rate > 0.5 in the molecular dynamics simulations of the M^{pro}-nirmatrelvir complexes. Atoms are labeled as "residue name@atom name".

	Atoms involved in hydrogen bonding to nirmatrelvir
Wild Type	GLU166@N, GLU166@O, HIE164@O, HIE163@NE2, CYS145@N
SER144ALA	GLU166@N, GLU166@O, HIE163@NE2
MET165ALA	GLU166@N, GLU166@O, THR190@N, HIE163@NE2
GLU166ALA	ALA166@N, ALA166@O, PHE140@O, HIE163@NE2
HIE172ALA	GLU166@N, GLU166@O, HIE164@O, HIE163@NE2
GLN192ALA	GLU166@N, GLU166@O, THR190@N, HIE163@NE2

The correlation between computational methods and experimental data in binding free energy calculations was analyzed using Pearson correlation coefficients. For MM/PBSA predictions, a weak correlation ($R_{Pearson}$ = 0.18) with experimental values was observed, indicating limited agreement. In contrast, Free Energy Perturbation (FEP) calculations employing Multistate Bennett Acceptance Ratio (MBAR) and Thermodynamic Integration (TI) demonstrated significantly stronger linear correlations, with Pearson coefficients of 0.56 and 0.57 respectively. These results highlight the enhanced accuracy achievable through FEP methods when combined with appropriate post-processing techniques, underscoring their superiority over MM/PBSA in capturing binding free energy trends accurately.

While the overall Pearson correlation coefficient for MM/PBSA is approximately 0.4 points lower than that of FEP, it has a significant cost advantage. Specifically, MM/PBSA requires only one 100-ns simulation to represent both bound and unbound ensembles, whereas FEP-based on Alchemical Free Energy (ABFE) method demands simulations for 33 alchemical windows, each running for 5 ns on a GPU. On an NVIDIA GeForce RTX 3080, the computational costs are substantial: FEP calculations take around 4.85 hours per GPU window, while MM/PBSA requires approximately 17.57 hours for simulation plus an additional 1.40 hours for post-processing using 32 CPU cores. For non-equilibrated simulations performed on CPUs (using Intel(R) Xeon(R) Gold 5320 CPUs @ 2.20 GHz), each 500 ps FEP window for the complex takes about 5.43 hours, with an additional 20 windows needed for the ligand, totaling 105.86 hours. In contrast, MM/PBSA requires only one simulation per complex.

In this study, the simplest and most commonly used MM/PBSA protocol is employed, incorporating two major approximations: neglecting the configurational entropy contribution to binding free energy and excluding explicit water molecules. Advanced MM/PBSA approaches, such as quasi-harmonic or normal-mode analysis[56], require significantly higher computational costs. Meanwhile, the FEP-based ABFE simulations in this study did not prioritize computational efficiency, leaving room for optimization in both setup preparation and simulation settings. Furthermore, utilizing user-friendly tools such as BFEE2 [76-78] and FEP-SPell-ABFE [79], which automate ABFE workflows and minimize human intervention, facilitates the calculations of ABFE.

4. Conclusion

This study assesses nirmatrelvir resistance in the SARS-CoV-2 main protease M^{pro} by examining the loss of binding affinity using the application of Molecular Mechanics/Poisson-Boltzmann Surface Area (MM/PBSA) and Free Energy Perturbation (FEP) based Absolute Binding Free Energy (ABFE) methods. The results can be summarized as follows: (1) FEP calculations exhibit stronger correlations with experimental affinities compared to MM/PBSA, highlighting their potential for precise determination of protein-ligand binding energies, especially when analyzing differences in binding energy across sequences. (2) Given lower computational expense, MM/PBSA methods remain valuable,

particularly when precise agreement with experimental absolute affinities is not critical. (3) The comparative study presented in this work advocates for the judicious application of MM/PBSA approximations in computational studies of protein-ligand binding interactions. While MM/PBSA maintains computational efficiency, its inherent limitations necessitate careful consideration of application scenarios. For instance, when computational resources are moderate, MM/PBSA is well suited to quickly generate approximate rankings of a large number of complexes in the pre-screening stage. In contrast, FEP offers greater accuracy in calculating protein-ligand binding free energies. Meanwhile, FEP calculations require strict adherence to established alchemical or geometric transformation protocols. It is also essential to perform a thorough convergence analysis of the simulation data to confirm the reliability and reproducibility of the results. Notably, while accuracy is a key strength of FEP, this accuracy depends critically on the quality and correctness of the initial given structure. In this work, the absence of crystal structures for the mutants necessitated structural optimization based on the wildtype crystal structure, which required comparatively long molecular dynamics simulations to reach the equilibrium of the mutant structure; shorter simulations risked inadequate representation of the mutant structure. In the future, integrating AI-driven techniques with FEP could efficiently reduce computational costs and maximize the value and potential of FEP.

Supporting information

The online version contains supplementary material available at website https://global-sci.com/storage/self-storage/cicc-2025-97-1-r1-si.pdf

References

[1] Richman, D. D.; Nathanson, N. In *Viral Pathogenesis*, Elsevier, (2016), 271-287.

[2] Carey, I.; Harrison, P. M. Monotherapy versus combination therapy for the treatment of chronic hepatitis B. *Expert Opin. Invest. Drugs*, **18** (2009), 1655-1666.

[3] Strasfeld L., Chou, S. Antiviral drug resistance: mechanisms and clinical implications. *Infect. Dis. Clin. North Am.*, **24** (2010), 413.

[4] Havranek B., Demissie, R., Lee H., Lan S.; Zhang H., Sarafianos S., Ayitou A. J.-L., Islam S. M. Discovery of nirmatrelvir resistance mutations in SARS-CoV-2 3CLpro: a computational-experimental approach. *J. Chem. Inf. Model.*, **63** (2023), 7180-7188.

[5] Hou T., Yu R. Molecular dynamics and free energy studies on the wild-type and double mutant HIV-1 protease complexed with amprenavir and two amprenavir-related inhibitors: Mechanism for binding and drug resistance. *J. Med. Chem.*, **50** (2007), 1177-1188.

[6] Wang E., Sun H., Wang J., Wang Z., Liu H., Zhang J. Z., Hou T. End-point binding free energy calculation with MM/PBSA and MM/GBSA: strategies and applications in drug design. *Chem. Rev.*, **119** (2019), 9478-9508.

[7] Li Z., Huang Y., Wu Y., Chen J., Wu D., Zhan C.-G., Luo H.-B. Absolute binding free energy calculation and design of a subnanomolar inhibitor of phosphodiesterase-10. *J. Med. Chem.*, **62** (2019), 2099-2111.

[8] Li Z., Li X., Huang Y.-Y., Wu Y., Liu R., Zhou L., Lin Y., Wu D., Zhang L., Liu H., Xu X., Yu K., Zhang Y., Cui J., Zhan C.-G., Wang X., Luo H.-B. Identify potent SARS-CoV-2 main-protease inhibitors via accelerated free-energy-perturbationbased virtual screening of existing drugs. *Proc. Natl. Acad. Sci. U.S.A.*, **117** (2020), 27381-27387.

[9] Li Z., Jiang M.-Y., Liu R., Wang Q., Zhou Q., Huang Y.-Y., Wu Y., Zhan C.-G., Luo H.-B. Discovery of highly potent phosphodiesterase-1 inhibitors by a combinedstructure free-energy-perturbation approach. *Acta Pharm. Sin. B*, **14** (2024), 5357-5369.

[10] Zhao Y., Fang C., Zhang Q., Zhang R., Zhao X., Duan Y., Wang H., Zhu Y., Feng L., Zhao J., Shao M., Yang X., Zhang L., Peng C., Yang K., Ma D., Rao Z., Yang H. Crystal structure of SARS-CoV-2 main protease in complex with protease inhibitor PF-07321332. *Protein Cell*. **13** (2022), 689-693.

[11] Gil C., Ginex T., Maestro I., Nozal V., Barrado-Gil L., Cuesta-Geijo M. Á., Urquiza J., Ramírez D., Alonso C., Campillo N. E., Martinez A. COVID-19: drug targets and potential treatments. *J. Med. Chem.*, **63** (2020), 12359-12386.

[12] Lu R., Zhao X., Li J., Niu P., Yang B., Wu H., Wang W., Song H., Huang B., Zhu N., Bi Y., Ma X., Zhan F., Wang L., Hu T., Zhou H., Hu Z., Zhou W., Zhao L., Chen J., …Tan, W. Genomic characterisation and epidemiology of 2019 novel coronavirus: Implications for virus origins and receptor binding. *Lancet*. **395** (2020), 565-574.

[13] Thiel V., Ivanov K. A., Putics A., Hertzig T., Schelle B., Bayer S., Weißbrich B., Snijder E. J., Rabenau H., Doerr H. W., Gorbalenya A. E., Ziebuhr J. Mechanisms and enzymes involved in SARS-coronavirus genome expression. *J. Gen. Virol.*, **84** (2003), 2305-2315.

[14] Ziebuhr J., Heusipp G., Siddell S. G. Biosynthesis, purification, and characterization of the human coronavirus 229E 3C-like proteinase. *J. Virol.*, **71** (1997), 3992-3997.

[15] Wang F., Chen C., Tan W., Yang K., Yang H. Structure of main protease from human coronavirus NL63: Insights for wide-spectrum anti-coronavirus drug design. *Sci. Rep.*, **6** (2016), 22677.

[16] Jin Z., Du X., Xu Y., Deng Y., Liu M., Zhao Y., Zhang B., Li X., Zhang L., Peng C., … Yang H. Structure of M^{pro} from SARS-CoV-2 and discovery of its inhibitors. *Nature*, **582** (2020), 289-293.

[17] Quan B.-X., Shuai H., Xia A.-J., Hou Y., Zeng R., Liu X.-L., … Yang S. An orally available M^{pro} inhibitor is effective against wild-type SARS-CoV-2 and variants including Omicron. *Nat. Microbiol.*, **7** (2022), 716-725.

[18] Qiao J., Li Y.-S., Zeng R., Liu F.-L., Luo R.-H., Huang C., … Yang S. SARS-CoV-2 M^{pro} inhibitors with antiviral activity in a transgenic mouse model. *Science*, **371** (2021), 1374-1378.

[19] Owen D. R., Allerton C. M., Anderson A. S., Aschenbrenner L., Avery M., … Zhu Y. An oral SARS-CoV-2 M^{pro} inhibitor clinical candidate for the treatment of COVID-19. *Science*, **374** (2021), 1586-1593.

[20] Zhang C.-H., Stone E. A., Deshmukh M., Ippolito J. A., Ghahremanpour M. M., … Jorgensen W. L. Potent noncovalent inhibitors of the main protease of SARS-CoV-2 from molecular sculpting of the drug perampanel guided by free-energy-perturbation calculations. *ACS Cent. Sci.*, **7** (2021), 467-475.

[21] Havranek B., Islam S. M. An in silico approach for identification of novel inhibitors as potential therapeutics targeting COVID-19 main protease. *J. Biomol. Struct. Dyn*., **39** (2021), 4304-4315.

[22] Duveau D. Y., Thomas C. J. The remarkable selectivity of nirmatrelvir. *ACS Pharmacol*. *Transl. Sci*., **5** (2022), 445-447.

[23] Hammond J., Leister-Tebbe H., Gardner A., Abreu P., Bao W., … Rusnak J. M. Oral nirmatrelvir for high-risk, non-hospitalized adults with COVID-19. *N. Engl. J. Med*., **386** (2022) , 1397-1408.

[24] Amani B., Amani B. Efficacy and safety of nirmatrelvir/ritonavir (Paxlovid) for COVID-19: a rapid review and meta-analysis. *J. Med. Virol*., **95** (2023) , e28441.

[25] Zhou Y., Gammeltoft K. A., Ryberg L. A., Pham L. V., Tjørnelund H. D., … Gottwein J. M. Nirmatrelvir-resistant SARS-CoV-2 variants with high fitness in an infectious cell-culture system. *Sci. Adv*., **8** (2022), eadd7197.

[26] Jochmans D., Liu C., Donckers K., Stoycheva A., Boland S., … Vandyck K. The substitutions L50F, E166A and L167F in SARS-CoV-2 3CLpro are selected by a protease inhibitor in vitro and confer resistance to nirmatrelvir. *MBio*, **14** (2023), e02815-22.

[27] Iketani S., Mohri H., Culbertson B., Hong S. J., Duan Y., … Ho D. D. Multiple pathways for SARS-CoV-2 resistance to nirmatrelvir. *Nature*, **613** (2023), 558-564.

[28] Moghadasi S. A., Heilmann E., Khalil A. M., Nnabuife C., Kearns F. L., … Harris R. S. Transmissible SARS-CoV-2 variants with resistance to clinical protease inhibitors. *Sci. Adv*., **9** (2023), eade8778.

[29] Hu Y., Lewandowski E. M., Tan H., Zhang X., Morgan R. T., … Wang J. Naturally occurring mutations of SARS-CoV-2 main protease confer drug resistance to nirmatrelvir. *ACS Cent. Sci*., **9** (2023), 1658-1669.

[30] Ullrich S., Ekanayake K. B., Otting G., Nitsche C. Main-protease mutants of SARS-CoV-2 variants remain susceptible to nirmatrelvir. *Bioorg. Med. Chem. Lett*., **62** (2022), 128629.

[31] Biovia D. S., Berman H., Westbrook J., Feng Z., Gilliland G., Bhat T., Richmond T. *Discovery Studio Visualizer* v.17.2. Dassault Systèmes, San Diego (2016).

[32] Frisch M. J., Trucks G. W., Schlegel H. B., Scuseria G. E., Robb M. A., … Fox D. J. *Gaussian 16* Rev. C.01. Gaussian Inc., Wallingford CT (2016).

[33] Wang J., Wolf R. M., Caldwell J. W., Kollman P. A., Case D. A. Development and testing of a general AMBER force field. *J. Comput. Chem*., **25** (2004), 1157-1174.

[34] Jakalian A., Bush B. L., Jack D. B., Bayly C. I. Fast, efficient generation of high-quality atomic charges. AM1-BCC model: I. method. *J. Comput. Chem*., **21** (2000), 132-146.

[35] Jakalian A., Jack D. B., Bayly C. I. Fast, efficient generation of high-quality atomic charges. AM1-BCC model: II. parameterization and validation. *J. Comput. Chem*., **23** (2002), 1623-1641.

[36] Maier J. A., Martinez C., Kasavajhala K., Wickstrom L., Hauser K. E., Simmerling C. ff14SB: improving the accuracy of protein side-chain and backbone parameters from ff99SB. *J. Chem. Theory Compu*t., **11** (2015), 3696-3713.

[37] Cieplak P., Cornell W. D., Bayly C., Kollman P. A. Application of the multimolecule and multiconformational RESP methodology to biopolymers: charge derivation for DNA, RNA and proteins. *J. Comput. Chem*., **16** (1995), 1357-1377.

[38] Case D. A., Aktulga H. M., Belfon K., Cerutti D. S., Cisneros G. A., … Merz K. M. Jr. AmberTools. *J. Chem. Inf. Model*., **63** (2023), 6183-6191.

[39] Ryckaert J.-P., Ciccotti G., Berendsen H. J. Numerical integration of the cartesian equations of motion of a system with constraints: molecular dynamics of n-alkanes. *J. Comput. Phys.*, **23** (1977), 327-341.

[40] Darden T., York D., Pedersen L. Particle-mesh Ewald: an N log (N) method for Ewald sums in large systems. *J. Chem. Phys*., **98** (1993), 10089-10092.

[41] Essmann U., Perera L., Berkowitz M. L., Darden T., Lee H., Pedersen L. G. A smooth particle-mesh Ewald method. *J. Chem. Phys*., **103** (1995), 8577-8593.

[42] Swanson J. M., Henchman R. H., McCammon J. A. Revisiting free-energy calculations: a theoretical connection to MM/PBSA and direct calculation of the association free energy.*Biophys. J*., **86** (2004), 67-74.

[43] Kollman P. A., Massova I., Reyes C., Kuhn B., Huo S., Chong L., … Cheatham T. E. Calculating structures and free energies of complex molecules: combining molecular mechanics and continuum models. *Acc. Chem. Res.*, **33** (2000), 889-897.

[44] Massova I., Kollman P. A. Combined molecular-mechanical and continuum-solvent approach (MM-PBSA/GBSA) to predict ligand binding. *Perspect. Drug Discovery Des*., **18** (2000), 113-135.

[45] Nicholls A., Honig B. A rapid finite-difference algorithm utilizing successive over-relaxation to solve the Poisson-Boltzmann equation. *J. Comput. Chem*., **12** (1991), 435-445.

[46] Massova I., Kollman P. A. Computational alanine scanning to probe protein-protein interactions: a novel approach to evaluate binding free energies. *J. Am. Chem. Soc*., **121** (1999), 8133-8143.

[47] Genheden S., Ryde U. The MM/PBSA and MM/GBSA methods to estimate ligand-binding affinities. *Expert Opin. Drug Discovery*, **10** (2015), 449-461.

[48] Homeyer N., Gohlke H. Free-energy calculations by the molecular-mechanics Poisson–Boltzmann surface-area method. *Mol. Inf*., **31** (2012), 114-122.

[49] Kumari R., Kumar R., Consortium O. S. D. D., Lynn A. g_mmpbsa: a GROMACS tool for high-throughput MM-PBSA calculations. *J. Chem. Inf. Model*., **54** (2014), 1951-1962.

[50] Gilson M. K., Zhou H.-X. Calculation of protein-ligand binding affinities. *Annu. Rev. Biophys. Biomol. Struct*., **36** (2007), 21-42.

[51] Miller B. R. III, McGee T. D. Jr, Swails J. M., Homeyer N., Gohlke H., Roitberg A. E. MMPBSA.py: an efficient program for end-state free-energy calculations. *J. Chem. Theory Comput*., **8** (2012), 3314-3321.

[52] Baker N. A., Sept D., Joseph S., Holst M. J., McCammon J. A. Electrostatics of nanosystems: application to microtubules and the ribosome. *Proc. Natl. Acad. Sci. U.S.A*., **98** (2001), 10037-10041.

[53] Srinivasan J., Cheatham T. E., Cieplak P., Kollman P. A., Case D. A. Continuum-solvent studies of the stability of DNA, RNA and phosphoramidate-DNA helices. *J. Am. Chem. Soc*., **120** (1998), 9401-9409.

[54] Honig B., Nicholls A. Classical electrostatics in biology and

chemistry. *Science*, **268** (1995), 1144-1149.

[55] Still W. C., Tempczyk A., Hawley R. C., Hendrickson T. Semianalytical treatment of solvation for molecular mechanics and dynamics. *J. Am. Chem. Soc*., **112** (1990), 6127-6129.

[57] Hou T., Wang J., Li Y., Wang W. Assessing the performance of the MM/PBSA and MM/GBSA methods. 1. The accuracy of binding free-energy calculations based on molecular-dynamics simulations. *J. Chem. Inf. Model*., **51** (2011), 69-82.

[58] Weis A., Katebzadeh K., Söderhjelm P., Nilsson I., Ryde U. Ligand affinities predicted with the MM/PBSA method: dependence on the simulation method and the force field. *J. Med. Chem*., **49** (2006), 6596-6608.

[59] Aldeghi M., Bodkin M. J., Knapp S., Biggin P. C. Statistical analysis on the performance of molecular-mechanics Poisson–Boltzmann surface-area versus absolute binding-free-energy calculations: bromodomains as a case study. *J. Chem. Inf. Model*., **57** (2017), 2203-2221.

[60] Kollman P. Free-energy calculations: applications to chemical and biochemical phenomena. *Chem. Rev*., **93** (1993), 2395-2410.

[61] Hamelberg D., McCammon J. A. Standard free energy of releasing a localized water molecule from the binding pockets of proteins: double-decoupling method. *J. Am. Chem. Soc*., **126** (2004), 7683-7689.

[62] Chen W., Cui D., Jerome S. V., Michino M., Lenselink E. B., … Wang L. Enhancing hit discovery in virtual screening through absolute protein-ligand binding-free-energy calculations. *J. Chem. Inf. Model*., **63** (2023), 3171-3185.

[63] Deng Y., Roux B. Computations of standard binding-free energies with molecular-dynamics simulations. *J. Phys. Chem. B*, **113** (2009), 2234-2246.

[64] Aldeghi M., Heifetz A., Bodkin M. J., Knapp S., Biggin P. C. Accurate calculation of the absolute free energy of binding for drug molecules. *Chem. Sci*., **7** (2016), 207-218.

[65] Ries B., Alibay I., Anand N. M., Biggin P. C., Magarkar A. Automated absolute binding-free-energy calculation workflow for drug discovery. *J. Chem. Inf. Model*., **64** (2024), 5357-5364.

[66] Cournia Z., Allen B., Sherman W. Relative binding-free-energy calculations in drug discovery: recent advances and practical considerations. *J. Chem. Inf. Model*., **57** (2017), 2911-2937.

[67] Robo M. T., Hayes R. L., Ding X., Pulawski B., Vilseck J. Z. Fast free-energy estimates from λ-dynamics with bias-updated Gibbs sampling. *Nat. Commun*., **14** (2023), 8515.

[68] Steinbrecher T., Mobley D. L., Case D. A. Non-linear scaling schemes for Lennard-Jones interactions in free-energy calculations. *J. Chem. Phys*., **127** (2007).

[69] Steinbrecher T., Joung I., Case D. A. Soft-core potentials in thermodynamic integration: comparing one- and two-step transformations. *J. Comput. Chem*., **32** (2011), 3253-3263.

[70] Lee T.-S., Cerutti D. S., Mermelstein D., Lin C., LeGrand S., … York D. M. GPU-accelerated molecular dynamics and free-energy methods in Amber18: performance enhancements and new features. *J. Chem. Theory Comput*., **13** (2017), 3077-3084.

[71] Lee, T.-S.; Cerutti, D. S.; Mermelstein, D.; Lin, C.; LeGrand, S.; Giese, T. J.; Roitberg, A.; Case, D. A.; Walker, R. C.; York, D. M. GPU-accelerated molecular dynamics and free energy methods in Amber18: Performance enhancements and new features. *J. Chem. Inf. Model*., **58** (2018), 2043-2050.

[72] Zwanzig R. W. High-temperature equation of state by a perturbation method. I. non-polar gases. *J. Chem. Phys*., **22** (1954), 1420-1426.

[73] Kirkwood J. G. Statistical mechanics of fluid mixtures. *J. Chem. Phys*., **3** (1935), 300-313.

[74] Shirts M. R., Chodera J. D. Statistically optimal analysis of samples from multiple equilibrium states. *J. Chem. Phys*., **129** (2008), 124105.

[75] Klimovich P. V., Shirts M. R., Mobley D. L. Guidelines for the analysis of free-energy calculations. *J. Comput.-Aided Mol. Des*., **29** (2015), 397-411.

[76] Fu H., Chen H., Blazhynska M., Coderc de Lacam E. G., Szczepaniak F., … Chipot C. Accurate determination of protein-ligand standard binding free energies from molecular-dynamics simulations. *Nat. Protoc*., **17** (2022), 1114-1141.

[77] Fu H., Gumbart J. C., Chen H., Shao X., Cai W., Chipot C. BFEE: a user-friendly graphical interface facilitating absolute binding-free-energy calculations. *J. Chem. Inf. Model*., **58** (2018), 556-560.

[78] Fu H., Chen H., Cai W., Shao X., Chipot C. BFEE2: automated, streamlined, and accurate absolute binding-free-energy calculations. *J. Chem. Inf. Model*., **61** (2021), 2116-2123.

[79] Li P., Pu T., Mei Y. FEP-Spell-ABFE: an open-source automated alchemical absolute binding-free-energy calculation workflow for drug discovery. *J. Chem. Inf. Model*., **65** (2025), 2711-2721.